https://doi.org/10.5194/egusphere-2025-3317
Preprint. Discussion started: 31 July 2025

3D magnetotelluric forward modeling using an edge-based finite element method with a variant semi-unstructured conformal hexahedral mesh

Weerachai Sarakorn[1] and Phongphan Mukwachi[2]

[1]Department of Mathematics, Faculty of Science, Khon Kaen University, Khon Kaen, 40002, Thailand
[2]Department of Mathematics and Statistics, Faculty of Science and Technology, Sakon Nakhon Rajabhat University, Sakon Nakhon, 47000, Thailand

Correspondence: Weerachai Sarakorn (wsarakorn@kku.ac.th)

Abstract. This research presents the implementation of a semi-structured hexahedral mesh for the edge-based finite element method, which is utilized in solving 3D magnetotelluric (MT) modeling. The semi-unstructured hexahedral mesh comprises an unstructured quadrilateral mesh for the horizontal directions and an automatically generated non-uniform mesh for the vertical direction. The edge-based finite element approach, utilizing this mesh pattern, has been developed. We present, compare, and discuss the accuracy, efficiency, and flexibility of our MT forward modeling codes for various 3D models. Numerical experiments indicate that our approach provides good accuracy when local mesh refinement is applied around sites and within the focus zone, yielding superior results compared to the conventional edge-based finite element method with a standard structured hexahedral mesh. The reliability of the developed codes was confirmed through comparisons with analytical solutions, benchmark COMMEMI3D, and topographic models. Furthermore, our developed codes, which incorporate a semi-unstructured hexahedral mesh, exhibit valuable features, such as managing topographic and complex zones, and refining the local mesh for a 3D domain over a structured hexahedral mesh. However, they require fewer mesh data points, such as nodes and elements, within the mesh.

1 Introduction

3D Magnetotelluric (MT) forward modeling, the heart of 3D MT inversion, can be solved by many variant numerical techniques such as the integral equation (IE) approaches (Wannamaker, 1991; Avdeev et al., 1997; Avdeev, 2005), the staggered grid finite difference (SGFD) method (Mackie and Madden, 1994; Smith, 1996; Siripunvaraporn et al., 2002; Baba and Seama, 2002; Han et al., 2009), the edge-based finite element (EBFE) methods (Mitsuhata and Uchida, 2004; Nam et al., 2007; Liu et al., 2008; Han et al., 2009; Ren et al., 2013; Usui, 2015; Grayver and Kolev, 2015; Kordy et al., 2016; Zhang et al., 2021), the staggered-grid finite volume (SGFV) approaches (Haber et al., 2000; Haber and Ascher, 2001), and the hybrid finite difference-finite element (HFDFE) approach (Varılsüha, 2024). Their accuracy, efficiency, and validity have been presented, compared, and discussed. In the early era, the IE method, based on applying Green's function to the scattering equation, and the SGFD, a variant of the SGFD method that enforces the continuity of electric current along the block's edges and across its faces (Yee,

https://doi.org/10.5194/egusphere-2025-3317
Preprint. Discussion started: 31 July 2025

1966; Siripunvaraporn et al., 2002), are accurate and efficient for the simple 3D domain. For a more complex computational domain with topography, bathymetry, or irregular subdomains, the computational loads increase dramatically because they rely more on the discretization or mesh to preserve the desired accuracy level. Furthermore, these methods are limited to rectangular discretization, which cannot effectively capture these crucial features in real-world situations.

For such complex 3D models, the modeling problems can be mitigated by utilizing the EBFE, SGFV, or HFDFE methods due to the flexibility of mesh type. These methods can effectively handle domains, including those with irregular interior structures. These characteristics render the latter two techniques similar and powerful for implementation in real geophysical domains. The SGFV method, a numerical approach for various conservation laws, is particularly appealing when the numerical flux is significant (Eymard et al., 2000). However, research advancements in electromagnetic (EM) modeling for the SGFV approach still need to catch up to those of the variant EBFE method. For the HFDFE scheme (Varılsüha, 2020), implementing MT inversion still requires numerous additional verifications.

As mentioned, the flexibility and advantages of the EBFE method rely on the type of mesh used. The choice of mesh type for the EBFE approach has a significant impact on both the quality and cost of the solution (Tadepalli et al., 2011; Schneider et al., 2022). Tetrahedral meshes are advantageous due to their automated generation capabilities for even the most complex geometries. Hexahedral meshes are often regarded as the gold standard due to their significant improvements in accuracy and computational efficiency. This benefit comes from the structure of the brick element, which provides more precise results with fewer nodes and is less susceptible to numerical errors, such as shear and volumetric locking, that can affect simulations involving bending or incompressible materials. This improved accuracy per element offers a clear advantage, as simulations can use fewer elements to achieve the desired precision, resulting in smaller models, reduced memory usage, and faster solutions. Such efficiency is particularly crucial in various modeling applications. However, this high performance comes with a significant challenge, as creating high-quality hexahedral mesh is still a difficult and often manual process, highlighting a fundamental trade-off between optimal simulation performance and the ease of automating tetrahedral meshing. Presently, implementations of structured and unstructured hexahedral meshes have garnered significant attention, and numerous surveys and discussions have been presented (Owen, 1998). For MT, EBFE approaches using a structured hexahedral mesh have been given, and their performance has been investigated (Mitsuhata and Uchida, 2004; Nam et al., 2007; Kordy et al., 2016; Zhang et al., 2021). The variant EBFE method with adaptive non-conformal unstructured hexahedral mesh has also been presented (Grayver and Kolev, 2015; Grayver, 2015). However, the EBFE approach, incorporating a variant conformal hexahedral mesh, remains both interesting and challenging for achieving better performance in 3D inversion.

In this study, we present 3D MT forward modeling using an alternative EBFE approach that employs a semi-structured hexahedral mesh. The semi-structured mesh algorithm consists of two subprocesses. The mesh in the two horizontal directions is generated with an automatic unstructured quadrilateral mesh algorithm, while the vertical dimension is created using an automatic nonuniform mesh algorithm. The variational principle is then applied to the EEBFE approximation. Consequently, a direct solver from the Scipy library in Python is used to solve the resulting system of equations, and the responses are estimated. Finally, we evaluate and discuss the efficiency and accuracy of our approach across various models, including half-space, COMMEMI3D, and topographic models.

https://doi.org/10.5194/egusphere-2025-3317
Preprint. Discussion started: 31 July 2025

2 Governing equations

In MT modeling, the displacement currents are negligible, and the electric current source is free. Assuming a time dependence $e^{-i\omega t}$, the electromagnetic phenomena are described by the first-order Maxwell's equations:

$$\nabla \times \mathbf{E} = i\omega\mu\mathbf{H}, \tag{1}$$

$$\nabla \times \mathbf{H} = \sigma\mathbf{E}, \tag{2}$$

where $\mathbf{E}$ and $\mathbf{H}$ are the electric and magnetic fields, respectively, ω is the angular frequency, μ is the magnetic permeability of free space, and σ is the conductivity. Solving the above-coupled system requires large memory storage (Mackie and Madden, 1994; Siripunvaraporn et al., 2002). The memory storage can be reduced significantly by solving the second-order equations. A decoupled second-order Maxwell's equation for $\mathbf{E}$ is expressed as

$$\nabla \times \nabla \times \mathbf{E} = i\omega\mu\sigma\mathbf{E} \text{ in } \Omega, \tag{3}$$

where Ω denotes the computing domain, including the air and earth layers. On the boundary, the tangential component (Harrington, 2001; Liu et al., 2008) is subjected to

$$\mathbf{E} \times \mathbf{n} = \mathbf{E}_0 \times \mathbf{n} \text{ on } \Gamma, \tag{4}$$

where Γ denotes the boundary of domain, $\mathbf{n}$ denotes the unit outward normal to the boundary and $\mathbf{E}_0$ denote the incident electric field on the boundary. For MT modeling, the source on the boundary can be classified into two cases. For the first case, we assume the source is parallel to the x-direction. This causes the induced magnetic field to be parallel to the y-direction. In another case, the source is parallel to the y-direction. This causes the induced magnetic field to be parallel to the x-direction. The first case is referred to as XY polarization, and the latter case is referred to as YX polarization. The graphical representation is illustrated in Figure 1.

3 Edge-based finite element method

3.1 Mesh algorithm: Semi-unstructured hexahedral elements

The mesh generation or discretization of the computational domain is the first step in the EBFE approach to solve equation (3), subject to the boundary condition as in equation (4), which includes the EBFE approach. A continuous 3D model, Ω, was meshed into multiple subdomains or elements, i.e., $\Omega = \cup_{e=1}^{M}\Omega^e$, where Ω^e is the e-th element and M is the total number of elements. For this work, all elements are hexahedra.

Typically, the MT domain Ω naturally composes air, irregular air-earth interfaces such as topography or bathymetry, and irregular subsurface with anomalies embedded within them. The structured hexahedral mesh can handle those by using a refinement mesh (Mitsuhata and Uchida, 2004; Nam et al., 2007; Kordy et al., 2016; Zhang et al., 2021). However, the refinement effects on the further subregions, i.e., the surplus small elements, appeared in the mesh. This also results in an excess of elements, and the distribution of the elements in the mesh does not smooth out as it should. This may result in a lower-quality

https://doi.org/10.5194/egusphere-2025-3317
Preprint. Discussion started: 31 July 2025

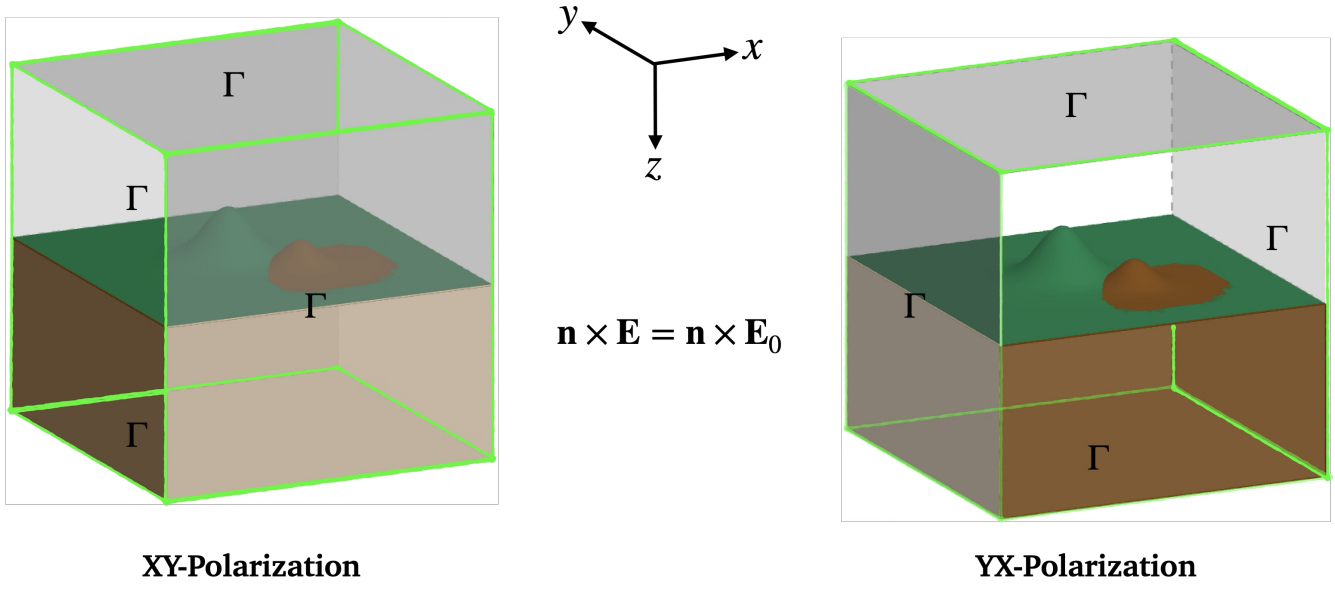

Figure 1. The boundary condition specifying on 3D domain for XY- and YX-polariztions.

mesh. Typically, producing high-quality mesh is essential for achieving optimal performance and accuracy in the FE Method when applied to the MT problem, as well-formed elements are crucial for stable numerical results and precise field representation (Jin, 2015). Our hybrid approach begins with creating a robust 2D unstructured quadrilateral mesh on the domain's horizontal projection using the paving algorithm. Paving's ability to generate high-quality, boundary-conforming quadrilateral meshes for any 2D shape (Blacker and Stephenson, 1991). The latest example of applying the paving algorithm to 2D MT domains can be found in Sarakorn (2017).

Starting from this 2D mesh, the 3D hexahedral mesh is created by extruding these quadrilateral elements vertically. Importantly, to accurately capture the significant resistivity contrasts and rapidly changing electromagnetic fields near the highly irregular topography and bathymetry, this extrusion uses an automatic, non-uniform layer thickness controlled by a fixed geometric growth rate. This adaptive vertical layering focuses mesh resolution where it's most needed – near the complex air-earth interface and other regions of expected high field gradients and penetration depth effects (Simpson and Bahr, 2005) – without excessively increasing the total element count across the large-scale domain. The coordinate interior of the mesh point in the vertical direction within the domain can be adjusted to handle irregularities. However, the number of mesh points remains fixed to match the number on the boundaries. The concept of this automatic non-uniform mesh in the vertical direction may be close to the previous EBFE approach, which utilized a structured hexahedral mesh (Nam et al., 2007; Kordy et al., 2016; Zhang et al., 2021).

By combining the geometric flexibility of a paving algorithm for the horizontal plane with controlled, adaptable vertical layering, this approach is expected to offer new and improved performance for 3D MT modeling through the EBFE approach,

https://doi.org/10.5194/egusphere-2025-3317
Preprint. Discussion started: 31 July 2025

providing more accurate solutions and better computational efficiency by effectively addressing electromagnetic fields across highly contrast geophysical structures, which are crucial for correct simulation of MT responses.

The example of a semi-unstructured mesh with linear elements for the 3D MT domain, based on the proposed concept, is illustrated in Figure 2.

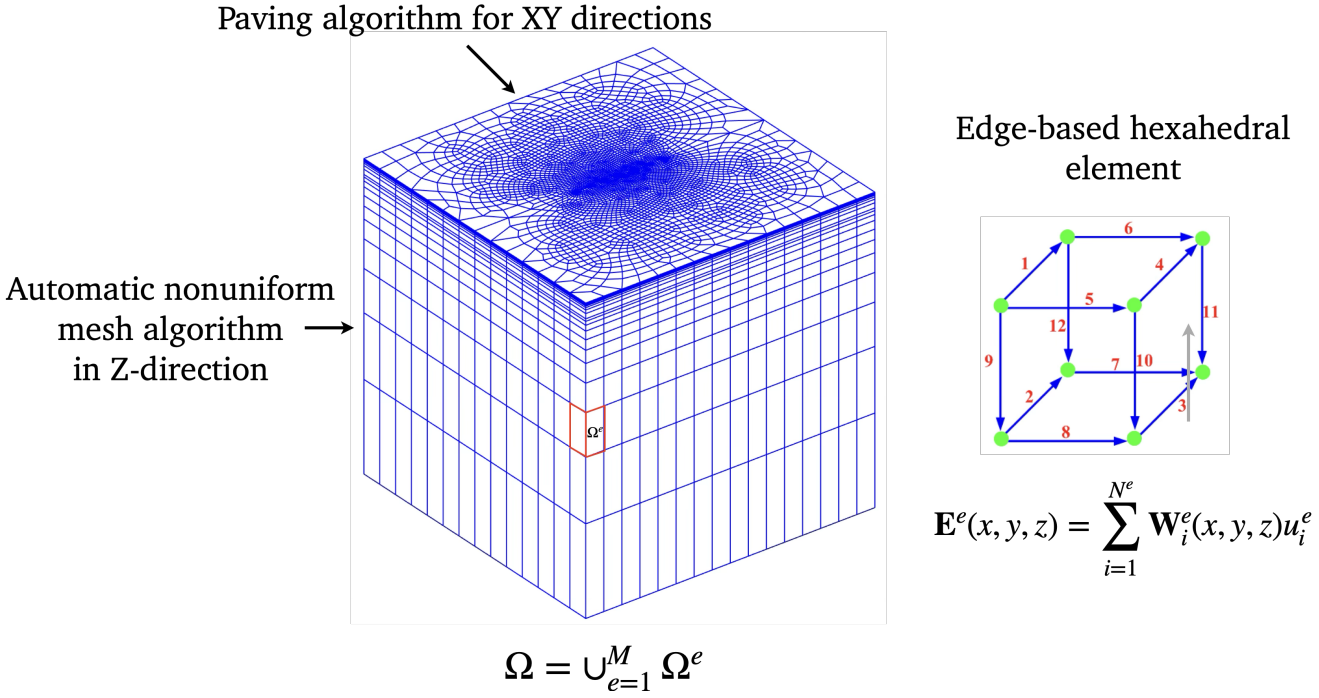

Figure 2. Example of meshing a 3D domain as a semi-unstructured hexahedral mesh with linear elements.

3.2 Variational method

Once the meshing process is complete, the mesh information is used for the EBFE approximation in the next step. To construct the formula, the boundary value problems in (3) are expressed as the variational formula

$$\mathbf{F}(\mathbf{E},\mathbf{V}) = g(\mathbf{V}), \mathbf{V} \in \mathbf{H}(curl;\Omega), \tag{5}$$

where $\mathbf{F}$ is the bilinear form, $\mathbf{H}(curl;\Omega)$ is the Sobolev space defined by $\mathbf{H}(curl;\Omega) = \{\mathbf{V} \in L^2(\Omega)^3 : \nabla \times \mathbf{V} \in L^2(\Omega)^3\}$ (Monk, 2003) and $\mathbf{V}$ is the test function. Applying the algebraic vector properties and Green's theorem (Nam et al., 2007; Liu et al., 2008), the (5) can be deduced as

$$\mathbf{F}(\mathbf{E},\mathbf{V}) = \int_{\Omega} [(\nabla \times \mathbf{E}) \cdot (\nabla \times \mathbf{V}) - i\omega\mu\sigma\mathbf{E} \cdot \mathbf{V}]\, d\Omega. \tag{6}$$

https://doi.org/10.5194/egusphere-2025-3317
Preprint. Discussion started: 31 July 2025

The Dirichlet boundary condition is regarded as the source term given by

$$\mathbf{g}(\mathbf{V}) = \int_{\Gamma} \mathbf{V} \cdot \mathbf{E}_0 d\Gamma, \tag{7}$$

where Γ is specified as the outer boundary of the domain. To solve the variational problem in (5), we discretize the domain Ω into distorted hexahedra, i.e.

$$\Omega = \bigcup_{e=1}^{M} \Omega_e, \tag{8}$$

where Ω^e is the eth hexahedral element and M is the total number of elements. The expression in equations (6) and (7) can be expressed, respectively, as

$$\mathbf{F}(\mathbf{E}, \mathbf{V}) = \sum_{e=1}^{M} \mathbf{F}^e(\mathbf{E}, \mathbf{V}), \tag{9}$$

$$\mathbf{g}(\mathbf{V}) = \sum_{e=1}^{M} \mathbf{g}^e(\mathbf{V}), \tag{10}$$

where

$$\mathbf{F}^e(\mathbf{E}, \mathbf{V}) = \int_{\Omega^e} [(\nabla \times \mathbf{E}) \cdot (\nabla \times \mathbf{V}) - i\omega\mu\sigma^e \mathbf{E} \cdot \mathbf{V}] \, d\Omega, \tag{11}$$

$$\mathbf{g}^e(\mathbf{V}) = \int_{\Gamma^e} \mathbf{V} \cdot \mathbf{E}_0 d\Gamma. \tag{12}$$

are defined over the Ω^e. For each Ω^e, the electric field is approximated by a linear combination of the basis functions given by

$$\mathbf{E}^e(x, y, z) = \sum_{i=1}^{N^e} \mathbf{W}_i^e(x, y, z) u_i^e, \tag{13}$$

where $\mathbf{W}_i^e(x, y, z)$ and u_i^e denote the vector basis function and the tangential electric field, respectively, on the ith edge of the eth element, and N^e is the number of edge per element (here, $N^e = 12$). The construction and expression of the vector basis functions for the hexahedral shape have been stated in several works (Volakis et al., 1998; Jin, 2015; Nam et al., 2007). Note that the construction of higher-order elements can be found in Grayver and Kolev (2015), and this can be applied to our mesh concept presented in this work. For this initiative, a first-order or linear element, as shown in Figure 2 (right), is used.

The expression for each vector basis function is more complicated when expressed in Cartesian coordinates (x, y, z). For simplicity, its expression will be expressed in the reference coordinate (u, v, w) by using a coordinate transformation between the distorted hexahedron and a 2-unit cubic. To continue the procedure, we substitute equation (13) into equation (11) and then select the test function as a vector basis function. Rearranging terms, the final expression of the coefficients in equations (11)

https://doi.org/10.5194/egusphere-2025-3317
Preprint. Discussion started: 31 July 2025

and (12) is given by

$$F_{ij}^{e} = \int_{\Omega'^{e}} \left[(\nabla \times \mathbf{W}_i^e) \cdot (\nabla \times \mathbf{W}_j^e) - i\omega\mu\sigma^e \mathbf{W}_i^e \cdot \mathbf{W}_j^e \right] |\mathbf{J}| d\Omega, \tag{14}$$

$$g_i^e = \int_{\Gamma'^{e}} \mathbf{W}_i^e \cdot \mathbf{E}_0 d\Gamma, \tag{15}$$

respectively. The appeared integrations are defined on reference coordinate, Ω'^{e} represents the 2-unit cubic, and Γ'^{e} represents the corresponding face of the cubic. The notation $|\mathbf{J}|$ is denoted as the determinant of the Jacobian matrix of transformation. The numerical integration technique is used to approximate those formulas. Here, we use the Gauss quadrature rule, as in Nam et al. (Nam et al., 2007). To complete the FE procedure, we assembled all elements to obtain the linear system of equations

$$\mathbf{K}\mathbf{u} = \mathbf{g}, \tag{16}$$

where $\mathbf{K}$ is a large, sparse, symmetric, and complex matrix but not Hermitian, $\mathbf{u}$ is the unknown vector, and $\mathbf{g}$ is the source vector corresponding to the Dirichlet boundary conditions. If the structured hexahedral is incorporated, the raised coefficient matrix $\mathbf{K}$ has at most 33 nonzero elements per equation. However, the maximum nonzero value is unpredictable when the semi-unstructured mesh is imposed. It depends on the mesh generation and density in some focus zones. The example of the sparse matrices for the EBFE with a structured and semi-unstructured mesh is shown in Figure 3. In practice, only nonzero elements are stored. The nonzero elements are stored by the Compressed Sparse Row (CSR) algorithm for our algorithm.

The system of equations in Equation (16) is solved using Krylov subspace solvers that incorporate preconditioning, as seen in several early works (Nam et al., 2007; Smith, 1996; Mitsuhata and Uchida, 2004; Liu et al., 2008). At that time, the direct solver, which consumes more memory resources, cannot be applied. With the availability of high-performance computing tools in the present, the direct solver is applicable (Kordy et al., 2016). Originally, our EBFE codes were developed under Fortran 90. With its widespread use and ecosystem for developers, Python has become a standard in scientific computing by combining a straightforward syntax with a high-performance library ecosystem, including NumPy and SciPy. These tools offer the speed of compiled C or Fortran code, enabling researchers to easily and efficiently orchestrate complex computations. Therefore, our code is wrapped and executed within a Python environment. Solving the system in (16) is performed using the NumPy package (Harris et al., 2020; The NumPy Developers, 2024) and the `scipy.sparse` module in the SciPy library (Harris et al., 2020; Virtanen et al., 2020; The NumPy Developers, 2024; The SciPy Developers, 2024).

Once the solution to the linear system of equations is obtained, the electric field at each MT site can be approximated using equation (13). In contrast, the magnetic field can be approximated using equation (3). The impedance, which is the ratio between the electric and perpendicular magnetic fields, is then calculated for each station. The relationship of this quantity for 3D cases is defined by

$$\begin{bmatrix} E_x^{xy} & E_x^{yx} \\ E_y^{xy} & E_y^{yx} \end{bmatrix} = \begin{bmatrix} Z_{xx} & Z_{xy} \\ Z_{yx} & Z_{yy} \end{bmatrix} \begin{bmatrix} H_x^{xy} & H_x^{yx} \\ H_y^{xy} & H_y^{yx} \end{bmatrix}, \tag{17}$$

https://doi.org/10.5194/egusphere-2025-3317
Preprint. Discussion started: 31 July 2025

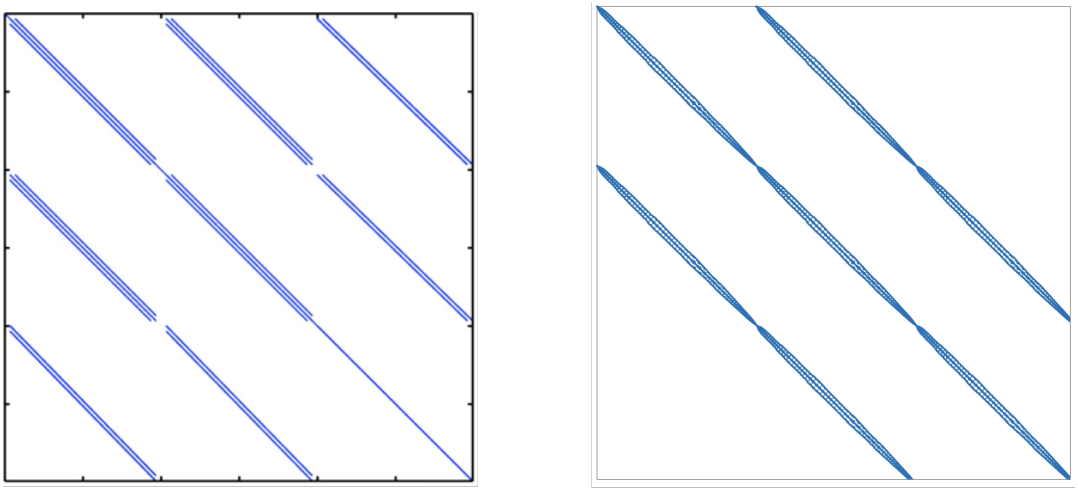

Figure 3. The sparsity pattern of nonzeros in sparse matrices generated by the EBFE approach with a structured (left) and semi-unstructured (right) mesh.

where the superscripts xy and yx are MT polarizations and the subscripts xx and yy are the horizontal components. The apparent resistivity and phase corresponding to the impedance can be calculated, respectively, by

$$\rho_{ij}^{a} = \frac{1}{\omega\mu}|Z_{ij}|^2, \tag{18}$$

and

$$\phi_{ij} = \arg(Z_{ij}), \tag{19}$$

where $i, j = x, y$, respectively.

4 Numerical results

This section will investigate the accuracy and efficiency of our EBFE approach with a semi-structured hexahedral mesh. The 3D models used here are the two-layered model, COMMEMI3D-2 (Zhdanov et al., 1997), and the trapezoidal hill models (Nam et al., 2007). The resistivity structures of the three models are shown in Figure 4. Note that the air layer is always needed for all models and is included in each selected model. The thickness of the air layer is set as 100 km, and its resistivity is set as 10^{10} ohm-m.

https://doi.org/10.5194/egusphere-2025-3317
Preprint. Discussion started: 31 July 2025

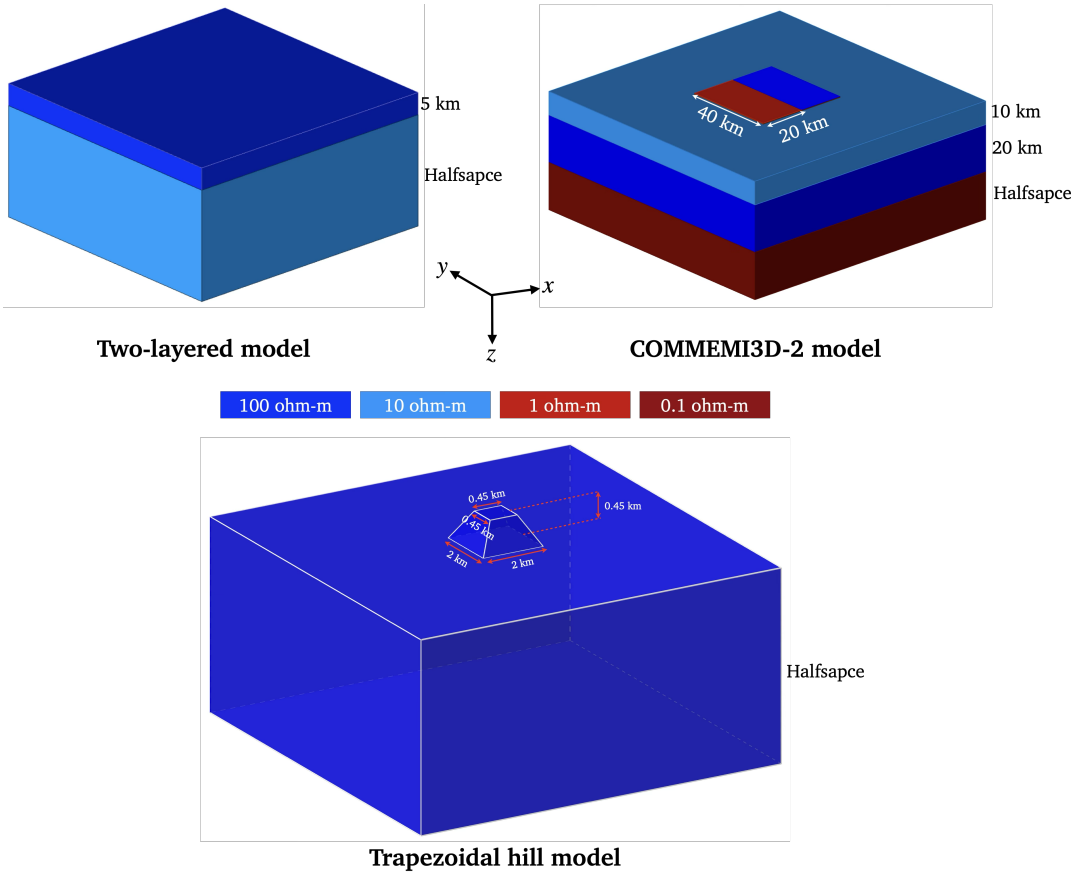

Figure 4. The 3D models used to validate and investigate the efficiency of our EBFE algorithm: two-layered model (left top), COMMEMI3D-2 model (right top), and Trapezoidal hill model (bottom).

4.1 Two-layered model

As shown in Figure 4, this model assumes that the earth's subsurface is flat, consisting of two layers. The thickness of the top layer and the bottom layer is 5 km, and the half-space, respectively. The corresponding resistivities are 100 ohm-m and 10 ohm-m, respectively. Therefore, the model's structure can be simplified to a one-dimensional structure, allowing for a comparison of the numerical results with those of existing analytical solutions (Constable et al., 1987). To simulate the responses, the computing domain is set to 100 km $\times$ 100 km $\times$ 200 km (air layer included). The 7 stations are designed to scatter in the South-East direction (from $x-$ to $x+$) around the model's center, with a distance of 5 km between each (See Figure 5). The periods of EM wave used in this case are 0.1, 1.0, 10, and 100 seconds.

For the meshing model, the smallest element size, defined as the minimum edge length of elements, is set to 30 m. The growth rate of element size, the approximate ratio between adjacent element sizes, is set to 1.5 for both algorithms. These

https://doi.org/10.5194/egusphere-2025-3317
Preprint. Discussion started: 31 July 2025

parameters played a crucial role in the accuracy of the methods. The comparison between the two mesh types is shown in Figure 5.

For the XY plane, both meshes around each station are refined to improve accuracy. As a result, the element density around and near each station is higher than in more distant regions. However, in the case of a semi-unstructured mesh created by a paving algorithm, the mesh's consistency is more flexible than that of a structured mesh generated by an automatic rectangular pattern. The mesh in the depth (z-direction) for both algorithms is identical for this research. The refinement is focused on the earth's surface and the layer interface, similar to the case of the XY plane. The number of mesh sections from the top air layer to the bottom of the earth is 29 sections. The summary of the mesh information and EBFE data for each type is shown in Table 1.

Table 1. Comparison of mesh information and EBFE data generated by structured and semi-unstructured hexahedral mesh algorithms for the two-layered model.

Mesh and FE data	**Structured mesh**	**Semi-unstructured mesh**
Num. of nodes	160650	128550
Num. of elements	149872	123366
Num. of unknowns	470955	417305
Size of matrix	470955×470955	417305×417305
Num. of nonzeros	13660875	12005513

With this condition, the density of elements in a structured hexahedral mesh is more significant than in a semi-unstructured hexahedral mesh. Furthermore, the edge-based FEM with a structured mesh consumes more memory storage than the one with an semi-unstructured mesh.

The accuracy of the obtained apparent resistivity and phase at each edge-based finite element method period with structured and semi-unstructured mesh algorithms is measured as the Mean absolute percentage error (MAPE) . For this model, the errors obtained by the two approaches are identical because the model's structure is 1-D, as mentioned, and both algorithms use the same mesh in depth. The mesh in all horizontal directions does not affect the errors. Furthermore, the mistakes in responses and polarizations remain consistent throughout each period. Figure 6 shows the errors for each period. The MAPE at each period is less than 1%.

Note that the apparent resistivity and phase of $XY-$ and $YX-$polarizations and all vertical magnetic transfer function components are less than 10^{-21}. Theoretically, these components are identical to zero for a 1-D structure (Simpson and Bahr, 2005). With the same level of accuracy, we observe that the EBFE approach with a semi-unstructured hexahedral mesh uses significantly fewer computational resources, such as storage of nonzero entries in the coefficient matrix, as shown in Table 1, compared to the structured hexahedral mesh case, which is less than about 12%.

https://doi.org/10.5194/egusphere-2025-3317
Preprint. Discussion started: 31 July 2025

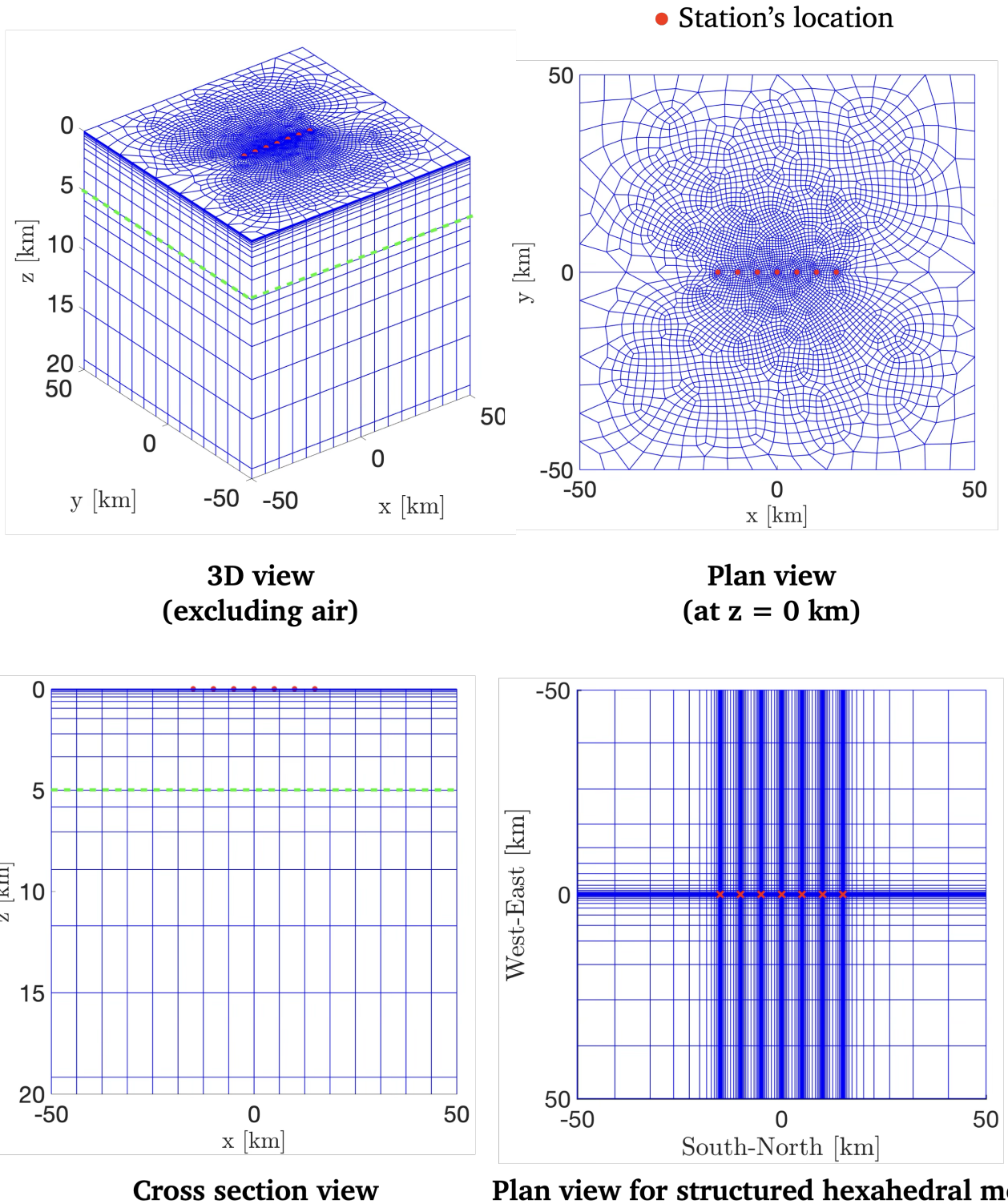

Figure 5. The semi-unstructured hexahedral mesh: 3D view at the surface $z = 0$ km excluding air (left top), top view (right top), and cross section view (left bottom), and the top view of the structure hexahedral mesh (right bottom). Note that the cross-section mesh of the two mesh types is set to be the same. The red dots are the locations of the stations.

https://doi.org/10.5194/egusphere-2025-3317
Preprint. Discussion started: 31 July 2025

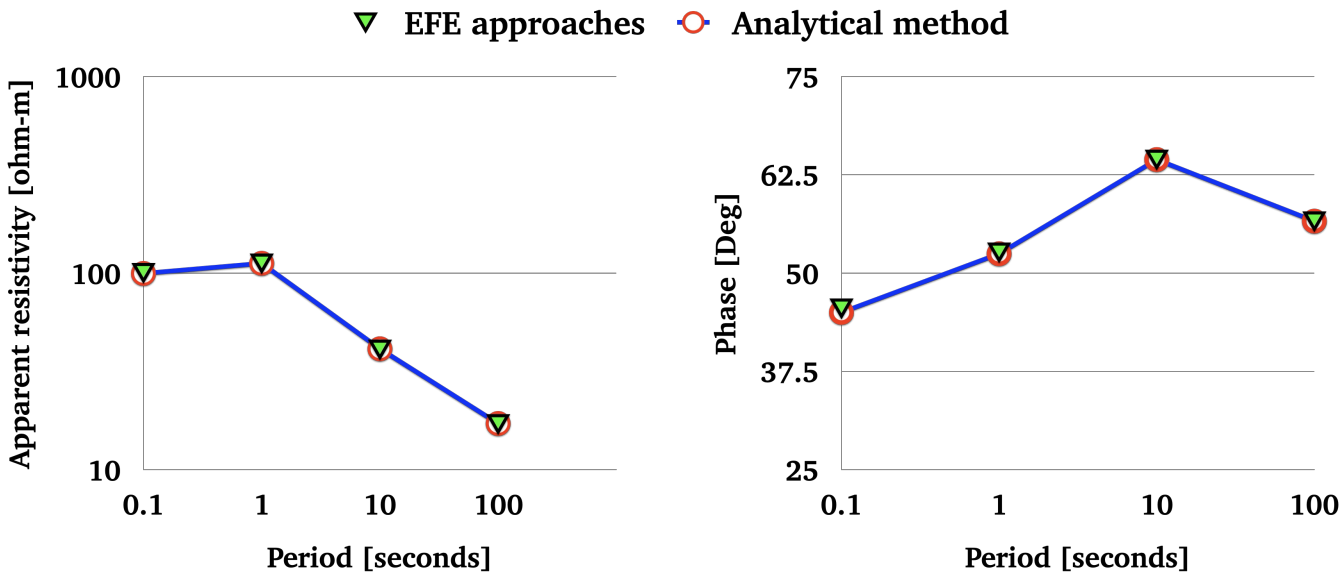

Figure 6. The percentage of errors for apparent resistivity and phase calculated by the EBFE with structured and unstructured hexahedral meshes.

4.2 COMMEMI3D-2 model

The COMMEMI3D-2 model is one of several 3D models created by the COMMEMI projects (Zhdanov et al., 1997). As shown in Figure 4, the COMMEMI3D-2 model assumes that the earth is flat and three-layered, with two anomalies embedded with different resistivities. The resistivity values for the top to bottom layers are 10 ohm-m, 100 ohm-m, and 0.1 ohm-m, respectively. The thicknesses of the top and middle layers are 10 km and 20 km, respectively. The bottom layer is semi-infinite. Two anomalies appeared embedded in the top layer with the exact sizes of 20 km $\times$ 40 km $\times$ 10 km. The resistivities for these two anomalies are 1 ohm-m and 100 ohm-m, respectively.

To perform the forward calculation, the computing domain size is set as 200 km $\times$ 200 km $\times$ 210 km (air included). As with COMMEMI3D projects, the locations of 15 stations with meshing domain by two approaches are shown in Figure 7.

The design of the mesh still uses the same concept from the previous model, i.e., mesh refinement is applied around stations and the interface. Additionally, the local refinement is also applied to the edges of the anomaly boundaries. Note that the number of vertical meth for two mesh types are 39 section. The summary of the mesh information and EBFE data is shown in Table 2.

According to Table 2, the computational resources used by EBFE with a semi-unstructured mesh are still designed to be less than those used by EBFE with a structured mesh by about 7%, to prove that the same accuracy level can be maintained for this model. Additionally, we present the CPU time required by each of our algorithms. The EBFE approach with a structured mesh takes 230 seconds for each polarization, which is longer than that of the EBFE approach with a semi-unstructured mesh, which

https://doi.org/10.5194/egusphere-2025-3317
Preprint. Discussion started: 31 July 2025

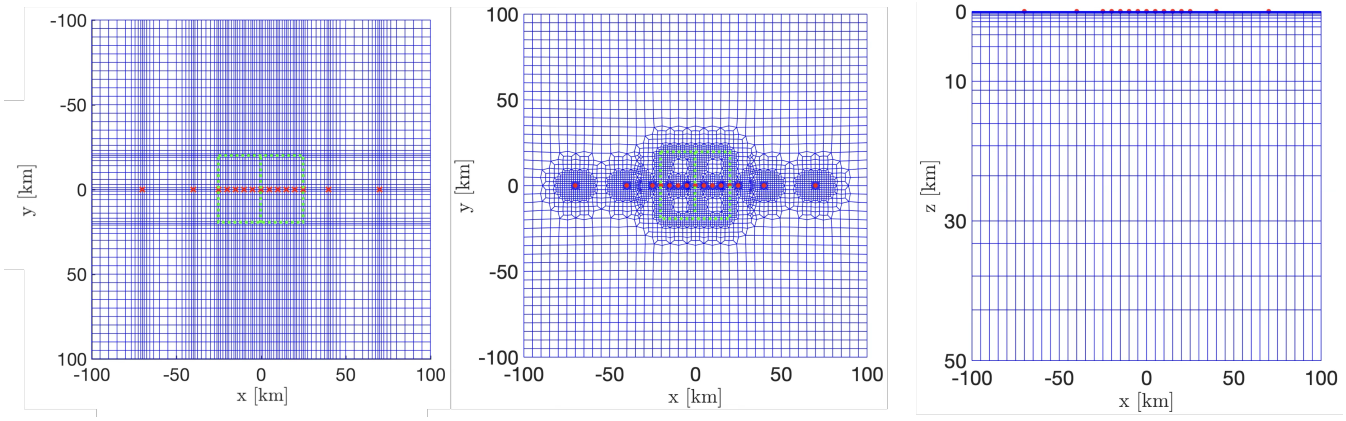

Figure 7. Meshing COMMEMI3D-2 model: top view of structured mesh (left), top view of semi-unstructured mesh (middle), cross-section view at -100 km (right). The 15 red dots are the locations of stations.

Table 2. Comparison of mesh information and EBFE data generated by structured and semi-unstructured hexahedral mesh algorithms for the COMMEMI3D-2model.

Mesh and FE data	Structured mesh	Semi-unstructured mesh
Num. of nodes	209880	188520
Num. of elements	198744	180648
Num. of unknowns	618313	575407
Size of matrix	618313×618313	575407×575407
Num. of nonzeros	18452073	17201779

takes 169 seconds. Note that this computation is performed on a MacBook Pro with an Intel Core i5, 2.3 GHz CPU, and 8.0 GB of RAM.

The comparison of apparent resistivity at period $T = 1,000$ seconds estimated by our two approaches and the COMMEMI project is shown in Figure 8. The graph of the MAPE is shown in Figure 9. The MAPE from the two approaches for XY-polarization is higher than that for YX-polarization. For each polarization, the MAPE of the EBFE approach with a structured mesh is lower than that of the EBFE approach with a semi-unstructured mesh, with less significance.

For the phase, the comparison of the apparent phase at a period of $T = 1,000$ seconds, estimated by our two approaches, is shown in Figure 10, while the COMMEMI projects do not present the phase in their experiments and are not shown in such a figure.

When we compute the MAPE of the EBFE approach using a semi-unstructured mesh, with the results from the structured mesh case as reference values, the obtained MAPEs are 0.60% and 0.45% for $XY-$ and $YX-$polarizations, respectively, which are too low and show no significant difference.

https://doi.org/10.5194/egusphere-2025-3317
Preprint. Discussion started: 31 July 2025

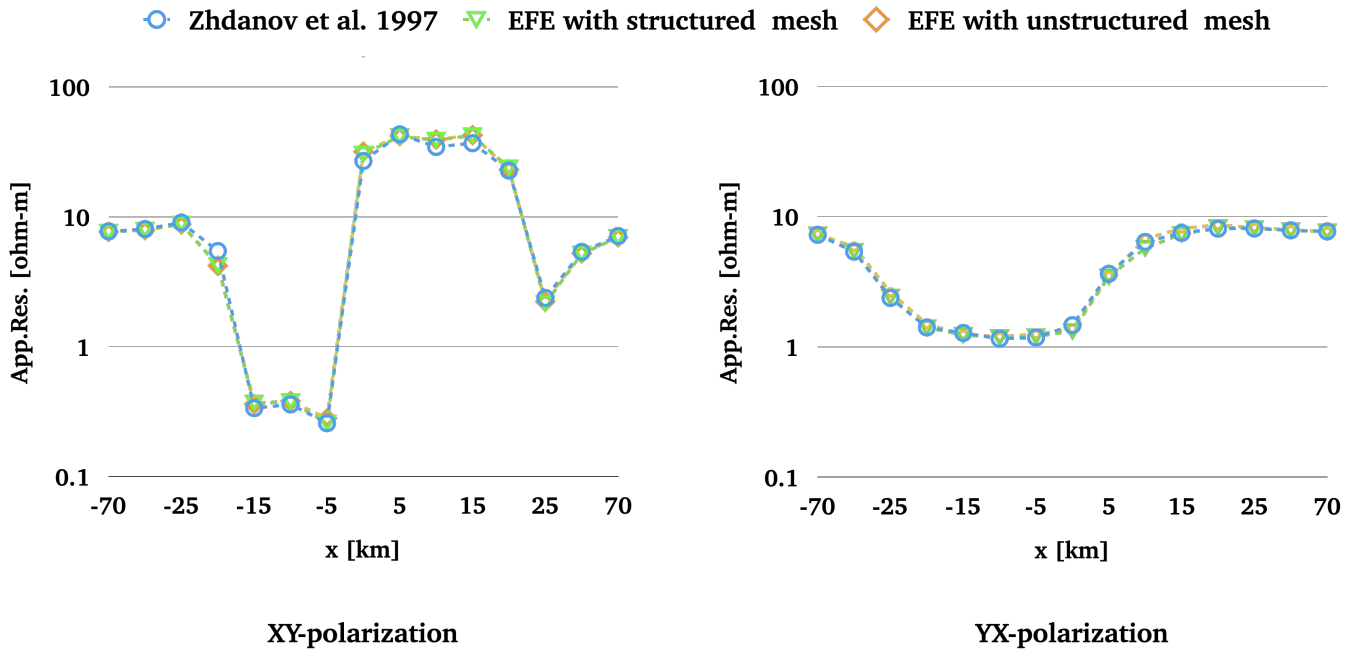

Figure 8. The comparison of apparent resistivity for $XY-$polarization (left) and $YX-$polarization (right) at period $T = 1,000$ seconds.

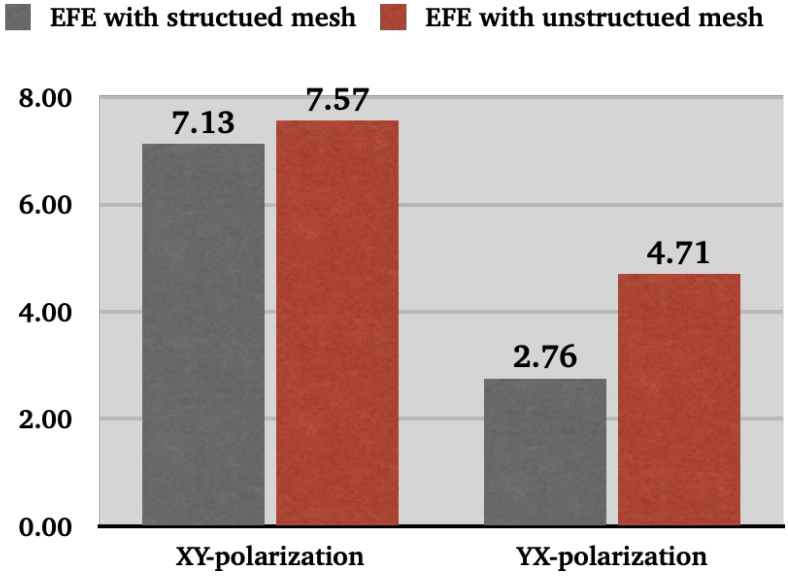

Figure 9. The calculated MAPE of apparent resistivity using the EBFE approach with structured and semi-unstructured data meshes.

https://doi.org/10.5194/egusphere-2025-3317
Preprint. Discussion started: 31 July 2025

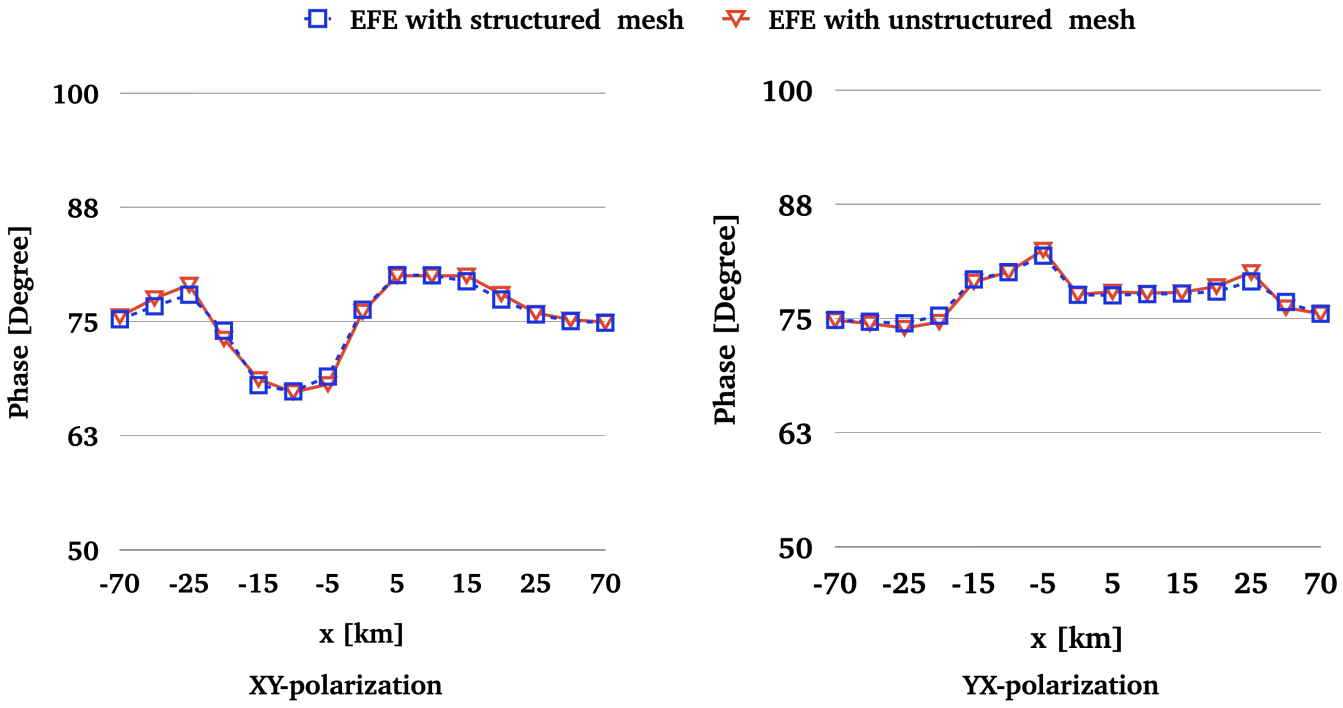

Figure 10. The comparison of phase for $XY-$polarization (left) and $YX-$polarization (right) at period $T = 1,000$ seconds.

With these metrics, the accuracy of our two approaches remains comparable, and their levels are nearly identical. However, the approach with a semi-unstructured mesh shows significantly better performance in terms of lower computational resource usage.

4.3 Trapezoidal hill model

The 3D Trapezoidal hill model (Nam et al., 2007) is an extension of the 2-D case (Wannamaker et al., 1986). As shown in Figure 4, the hill with a symmetric trapezoidal shape or truncated pyramid is designed at the center of the earth's surface, whereas elsewhere it is flat. It has a rectangular base with 2 km $\times$ 2 km, top side with 0.45 km $\times$ 0.45 km, and with height 0.45 km. The resistivity structure is 100 ohm-m halfspace. The meshing model using a semi-unstructured mesh is shown in Figure 11. The refinement is imposed around size and topographic zone. Semi-structured mesh handles the topographic zone very well, and the mesh density around this zone is also relaxed. Note that the z-coordinate of each mesh point located beneath and above the topographic zone is adjusted to preserve the mesh projection, and the mesh refinement is similar to that on the boundary.

To perform the computing, the domain is set as 40 km $\times$ 40 km $\times$ 150 km (air included). The responses from 26 stations are computed at 0.5 seconds and compared to those of Nam et al. (2007) and Wannamaker et al. (1986). The responses are plotted, compared, and displayed in Figure 12.

https://doi.org/10.5194/egusphere-2025-3317
Preprint. Discussion started: 31 July 2025

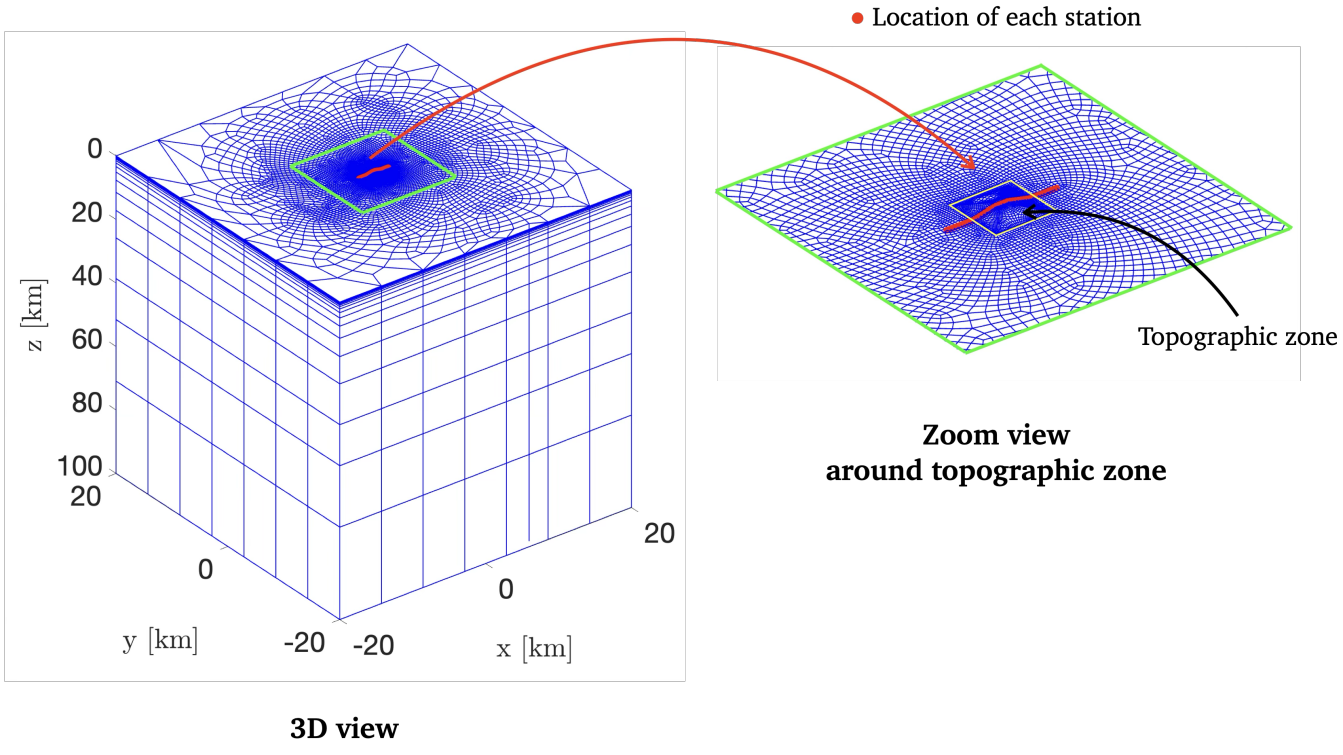

Figure 11. Meshing trapezoidal hill model: 3D mesh view (left) and zoom view around topographic zone (right). The 41 red dots are the locations of stations.

The results, the apparent resistivities and phase, indicate that the EBFE approach with a semi-structured mesh provides comparable responses to those calculated by the EBFE methods with a structured mesh (Nam et al., 2007; Wannamaker et al., 1986).

5 Discussion

In this study, we presented and carefully evaluated an alternative edge-based finite element (EBFE) method for 3D magnetotelluric (MT) forward modeling, characterized by its innovative use of a semi-unstructured hexahedral mesh. Our primary goal was to address ongoing challenges in 3D MT modeling, specifically balancing geometric flexibility, solution accuracy, and computational efficiency, especially when working with complex geological structures and the need for localized mesh refinement.

The proposed semi-unstructured hexahedral mesh, which combines an unstructured quadrilateral mesh for the horizontal directions (created using the paving algorithm) with an automatically generated non-uniform mesh for the vertical direction, showed significant benefits. This hybrid meshing approach was crucial for achieving better mesh quality and adaptability com-

https://doi.org/10.5194/egusphere-2025-3317
Preprint. Discussion started: 31 July 2025

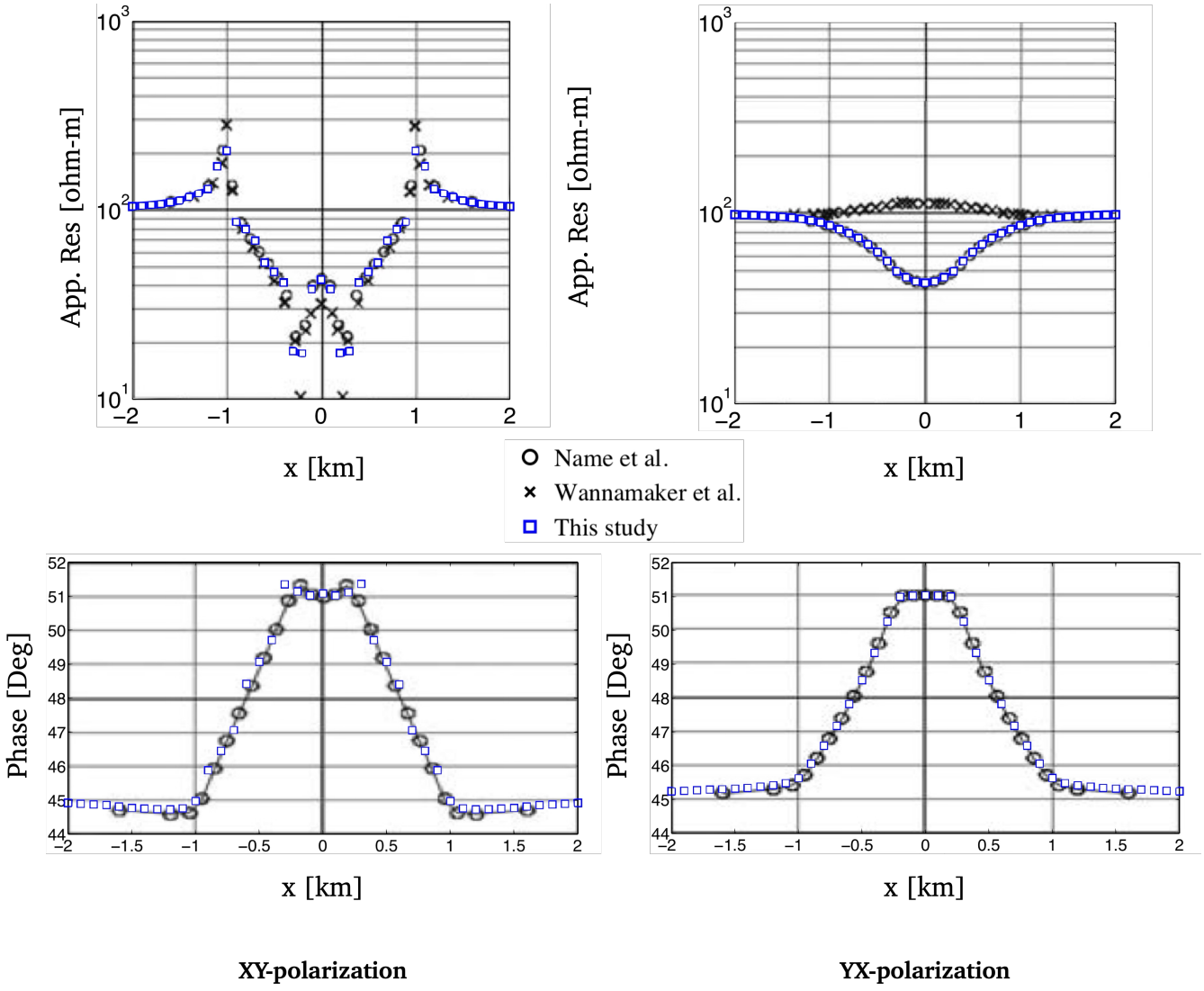

Figure 12. The comparison of responses at 0.5 seconds for trapezoidal hill model.

https://doi.org/10.5194/egusphere-2025-3317
Preprint. Discussion started: 31 July 2025

pared to traditional structured hexahedral meshes. As shown by numerical experiments on the two-layered and COMMEMI3D-2 models, our method consistently used a notably lower number of nodes and elements, and consequently, fewer non-zero entries in the resulting coefficient matrix. Specifically, for the two-layered model, we observed about 12% fewer data points, and for the COMMEMI3D-2 model, roughly 7% fewer, compared to the structured mesh versions (Tables 1 and 2). This reduction in mesh data directly decreases memory usage and accelerates computations, as further evidenced by the reduced CPU time for the COMMEMI3D-2 model (169 seconds with the semi-unstructured mesh versus 230 seconds with the structured mesh). The efficiency gains are primarily due to the targeted refinement capabilities of the semi-unstructured mesh, which limits the creation of "surplus small elements" in regions that do not require high resolution—an issue familiar with purely structured refinement methods.

Crucially, these efficiency improvements were achieved without compromising accuracy. For the 1D two-layered model, our approach yielded results with a Mean Absolute Percentage Error (MAPE) of less than 1% (Figure 6), identical to that of the structured mesh and in excellent agreement with analytical solutions. This confirms the fundamental correctness of the implementation even with reduced mesh density. In the more complex 3D COMMEMI3D-2 benchmark, the accuracy of our semi-unstructured EBFE method remained highly comparable to both the structured EBFE approach and established COMMEMI project results (Figure 8). The computed MAPEs for phase, when referenced against the structured mesh case (0.60% for XY-polarization and 0.45% for YX-polarization), further underscore the negligible difference in accuracy between the two meshing strategies (Figure 9). The successful validation against these well-known benchmarks confirms the reliability and robustness of our developed codes.

Furthermore, the flexibility of the semi-unstructured hexahedral mesh was clearly demonstrated by its ability to effectively manage and conform to complex topographic features, as shown with the trapezoidal hill model. As depicted in Figure 11, our method efficiently handles irregular air-earth interfaces, offering a more relaxed and optimized mesh density around these critical areas. Unlike IE or SGFD methods, which are often limited to rectangular discretization, our approach's adaptability makes it especially useful for realistic geophysical applications involving complex subsurface and surface geometries. Implemented within a Python environment using the NumPy and SciPy libraries to solve large, sparse systems of equations, this approach further improves the practicality and accessibility for the broader scientific community.

6 Conclusion

This research successfully developed and validated a 3D MT forward modeling approach utilizing an edge-based finite element (EBFE) method coupled with a novel semi-unstructured hexahedral mesh. This meshing strategy, which combines unstructured quadrilaterals in the horizontal plane with non-uniform vertical layering, proved to be highly effective. Our numerical experiments consistently demonstrated that this approach maintains high accuracy, yielding results in excellent agreement with analytical solutions, established benchmark models, and comparative studies against topographic models. The EBFE approach achieves superior computational efficiency, notably by requiring fewer nodes, elements, and non-zero entries in the system matrix compared to conventional structured hexahedral meshes, leading to reduced memory consumption and faster compu-

https://doi.org/10.5194/egusphere-2025-3317
Preprint. Discussion started: 31 July 2025

tation times. Additionally, our EBFE method exhibits enhanced flexibility in handling complex geological features, including topographic variations and localized anomalous zones, through its adaptive mesh refinement capabilities without introducing unnecessary mesh density.

The reliability and performance demonstrated by our developed codes position this EBFE approach, featuring a semi-unstructured hexahedral mesh, as a powerful and practical tool for advanced 3D MT forward modeling. Its ability to accurately and efficiently simulate MT responses in complex geological environments makes it an up-and-coming new option for future applications in 3D MT inversion, facilitating a more realistic and cost-effective interpretation of field data.

Author contributions. Weerachai Sarakon designed the original concept and methodology, developed the codes, drafted the initial manuscript, edited, and revised it. Phongphan Mukwachi assisted in conducting numerical experiments, collecting the results, and creating visualizations. All authors reviewed the manuscript.

Competing interests. The authors declare that they have no competing interests.

Acknowledgements. This work was supported by the National Research Council of Thailand and Khon Kaen University, Thailand (Grant Number 6200052)

https://doi.org/10.5194/egusphere-2025-3317
Preprint. Discussion started: 31 July 2025

References

Avdeev, D. B.: Three-dimensional electromagnetic modelling and inversion from theory to application, Surveys in Geophysics, 26, 767–799, https://doi.org/https://doi.org/10.1007/s10712-005-1836-x, 2005.

Avdeev, D. B., Kuvshinov, A. V., Pankratov, O. V., and Newman, G. A.: High-performance three-dimensional electromagnetic modelling using modified neumann series. Wide-Band numerical solution and examples, Journal of Geomagnetism and Geoelectricity, 49, 1519–1539, https://doi.org/https://doi.org/10.5636/jgg.49.1519, 1997.

Baba, K. and Seama, N.: A new technique for the incorporation of seafloor topography in electromagnetic modelling, Geophysical Journal International, 150, 392–402, https://doi.org/https://doi.org/10.1046/j.1365-246X.2002.01673.x, 2002.

Blacker, T. D. and Stephenson, M. B.: Paving. A new approach to automated quadrilateral mesh generation, International Journal for Numerical Methods in Engineering, 32, 811–847, https://doi.org/https://doi.org/10.1002/nme.1620320410, 1991.

Constable, S., Parker, R., and Constable, C.: Occam's inversion: a practical algorithm for generating smooth models from electromagnetic sounding data., Geophysics, 52, 289–300, https://doi.org/https://doi.org/10.1190/1.1442303, 1987.

Eymard, R., Gallouët, T., and Herbin, R.: Finite volume methods, Handbook of Numerical Analysis, 7, 713–1018, https://doi.org/10.1016/S1570-8659(00)07005-8, 2000.

Grayver, A. V.: Parallel three-dimensional magnetotelluric inversion using adaptive finite-element method. Part I: theory and synthetic study, Geophysical Journal International, 202, 584–603, 2015.

Grayver, A. V. and Kolev, T. V.: Large-scale 3D geoelectromagnetic modeling using parallel adaptive high-order finite element method, GEOPHYSICS, 80, E277–E291, https://doi.org/https://doi.org/10.1190/geo2015-0013.1, 2015.

Haber, E. and Ascher, U. M.: Fast finite volume simulation of 3D electromagnetic problems with highly discontinuous coefficients, SIAM Journal of Scientific Computing, 22, 1943–1961, https://doi.org/https://doi.org/10.1137/S1064827599360741, 2001.

Haber, E., Ascher, U. M., Aruliah, D. A., and Oldenburg, D. W.: Fast Simulation of 3D Electromagnetic Problems Using Potentials, Journal of Computational Physics, 163, 150–171, https://doi.org/https://doi.org/10.1006/jcph.2000.6545, 2000.

Han, N., Nam, M. J., Kim, H. J., Song, Y., and Suh, J. H.: A comparison of accuracy and computation time of three-dimensional magnetotelluric modelling algorithms, Journal of Geophysics and Engineering, 6, 136, https://doi.org/https://doi.org/10.1088/1742-2132/6/2/005, 2009.

Harrington, R. F.: Time-Harmonic electromagnetic fields, IEEE & Wiley, 2001.

Harris, C. R., Millman, K. J., van der Walt, S. J., Gommers, R., Virtanen, P., Cournapeau, D., Wieser, E., Taylor, J., Berg, S., Smith, N. J., Kern, R., Picus, M., Hoyer, S., van Kerkwijk, M. H., Brett, M., Haldane, A., del Río, J. F., Wiebe, M., Peterson, P., Gérard-Marchant, P., Sheppard, K., Reddy, T., Weckesser, W., Abbasi, H., Gohlke, C., and Oliphant, T. E.: Array programming with NumPy, Nature, 585, 357–362, https://doi.org/10.1038/s41586-020-2649-2, 2020.

Jin, J.: The Finite Element Method in Electromagnetics, John Wiley and Sons. Inc., 3rd edn., 2015.

Kordy, M., Wannamaker, P., Maris, V., Cherkaev, E., and Hill, G.: 3-D magnetotelluric inversion including topography using deformed hexahedral edge finite elements and direct solvers parallelized on SMP computers – Part I: forward problem and parameter Jacobians, Geophysical Journal International, 204, 74–93, https://doi.org/https://doi.org/10.1093/gji/ggv410, 2016.

Liu, C., Ren, Z., Tang, J., and Yan, Y.: Three-dimensional magnetotellurics modeling using edge-based finite-element unstructured meshes, Applied Geophysics, 5, 170–180, https://doi.org/https://doi.org/10.1007/s11770-008-0024-4, 2008.

https://doi.org/10.5194/egusphere-2025-3317
Preprint. Discussion started: 31 July 2025

Mackie, R. L. Smith, J. T. and Madden, T. R.: Three-dimensional electromagnetic modeling using finite difference equations: The magnetotelluric example, Radio Science, 29, 923–935, https://doi.org/https://doi.org/10.1029/94RS00326, 1994.

Mitsuhata, Y. and Uchida, T.: 3D magnetotelluric modeling using the T-Ω finite-element method, Geophysics, 69, 108–119, https://doi.org/https://doi.org/10.1190/1.1649380, 2004.

Monk, P.: Finite element methods for Maxwell's equations, Oxford University Press, New York, 2003.

Nam, M. J., Kim, H. J., Song, Y., Lee, T. J., Son, J.-S., and Suh, J. H.: 3D magnetotelluric modelling including surface topography, Geophysical Prospecting, 55, 277–287, https://doi.org/https://doi.org/10.1111/j.1365-2478.2007.00614.x, 2007.

Owen, S. J.: A Survey of Unstructured Mesh Generation Technology, in: International Meshing Roundtable, pp. 239–267, 1998.

Ren, Z., Kalscheuer, T., Greenhalgh, S., and Maurer, H.: A goal-oriented adaptive finite-element approach for plane wave 3-D electromagnetic modelling, Geophysical Journal International, 194, 700–718, https://doi.org/https://doi.org/10.1093/gji/ggt154, 2013.

Sarakorn, W.: 2-D magnetotelluric modeling using finite element method incorporating unstructured quadrilateral elements, Journal of Applied Geophysics, 139, 16 – 24, https://doi.org/https://doi.org/10.1016/j.jappgeo.2017.02.005, 2017.

Schneider, T., Hu, Y., Gao, X., Dumas, J., Zorin, D., and Panozzo, D.: A Large-Scale Comparison of Tetrahedral and Hexahedral Elements for Solving Elliptic PDEs with the Finite Element Method, ACM Trans. Graph., 41, https://doi.org/10.1145/3508372, 2022.

Simpson, F. and Bahr, K.: Practical Magnetotellurics, chap. Basic theoretical concepts, Cambridge University Press, https://doi.org/https://doi.org/10.1017/CBO9780511614095, 2005.

Siripunvaraporn, W., Egbert, G., and Lenbury, Y.: Numerical accuracy of magnetotelluric modeling: A comparison of finite difference approximations, Earth, Planets and Space, 54, 721–725, https://doi.org/https://doi.org/10.1186/BF03351724, 2002.

Smith, J. T.: Conservative modeling of 3-D electromagnetic fields, Part II: Biconjugate gradient solution and an accelerator, Geophysics, 61, 1319–1324, https://doi.org/https://doi.org/10.1190/1.1444055, 1996.

Tadepalli, S. C., Erdemir, A., and Cavanagh, P. R.: Comparison of hexahedral and tetrahedral elements in finite element analysis of the foot and footwear, Journal of Biomechanics, 44, 2337–2343, https://doi.org/https://doi.org/10.1016/j.jbiomech.2011.05.006, 2011.

The NumPy Developers: NumPy, https://numpy.org, accessed: 2024-06-25, 2024.

The SciPy Developers: SciPy, https://scipy.org, accessed: 2024-06-25, 2024.

Usui, Y.: 3-D inversion of magnetotelluric data using unstructured tetrahedral elements: applicability to data affected by topography, Geophysical Journal International, 202, 828–849, https://doi.org/https://doi.org/10.1093/gji/ggv186, 2015.

Varılsüha, D.: 3D inversion of magnetotelluric data by using a hybrid forward-modeling approach and mesh decoupling, GEOPHYSICS, 85, E191–E205, https://doi.org/10.1190/geo2019-0202.1, 2020.

Varılsüha, D.: A novel hybrid finite element – Finite difference approach for 3D Magnetotelluric modeling, Computers & Geosciences, 188, 105 614, https://doi.org/https://doi.org/10.1016/j.cageo.2024.105614, 2024.

Virtanen, P., Gommers, R., Oliphant, T. E., Haberland, M., Reddy, T., Cournapeau, D., Burovski, E., Peterson, P., Weckesser, W., Bright, J., van der Walt, S. J., Brett, M., Wilson, J., Millman, K. J., Mayorov, N., Nelson, A. R. J., Jones, E., Kern, R., Larson, E., Carey, C. J., Polat, İ., Feng, Y., Moore, E. W., VanderPlas, J., Laxalde, D., Perktold, J., Cimrman, R., Henriksen, I., Quintero, E. A., Harris, C. R., Archibald, A. M., Ribeiro, A. H., Pedregosa, F., van Mulbregt, P., and SciPy 1.0 Contributors: SciPy 1.0: Fundamental Algorithms for Scientific Computing in Python, Nature Methods, 17, 261–272, https://doi.org/10.1038/s41592-019-0686-2, 2020.

Volakis, J. L., Chatterjee, A., and Kempel, L. C.: Finite Element Method for Electromagnetics: Antennas, microwave circuits, and scattering applications, John Wiley & Sons, Inc., 1998.

https://doi.org/10.5194/egusphere-2025-3317
Preprint. Discussion started: 31 July 2025

Wannamaker, P. E.: Advances in three-dimensional magnetotelluric modeling using integral equations, Geophysics, 56, 1716–1728, https://doi.org/https://doi.org/10.1190/1.1442984, 1991.

Wannamaker, P. E., Stodt, J. A., and Rijo, L.: Two-dimensional topographic responses in magnetotellurics modeled using finite elements., Geophysics, 51, 2131–2144, https://doi.org/https://doi.org/10.1190/1.1442065, 1986.

Yee, K. S.: Numerical solution of initial boundary value problems involving Maxwell's equations in isotropic media, IEEE. Trans. Anten. Propag., AP-14, 302–307, https://doi.org/https://doi.org/10.1109/TAP.1966.1138693, 1966.

Zhang, J., Liu, J., Feng, B., Zheng, Y., Guan, J., and Liu, Z.: Three-dimensional magnetotelluric modeling using the finite element model reduction algorithm, Computers & Geosciences, 151, 104 750, https://doi.org/https://doi.org/10.1016/j.cageo.2021.104750, 2021.

Zhdanov, M. S., Varentsov, I. M., Weaver, J. T., Golubev, N. G., and Krylov, V. A.: Methods for modelling electromagnetic fields Results from COMMEMI-The international project on the comparison of modelling methods for electromagnetic induction, Journal of Applied Geophysics, 37, 133–271, https://doi.org/https://doi.org/10.1016/S0926-9851(97)00013-X, 1997.